ACS APPLIED MATERIALS & INTERFACES

Research Article

Cite This: ACS Appl. Mater. Interfaces 2018, 10, 1084−1092

www.acsami.org

Carbon Dots/Prussian Blue Satellite/Core Nanocomposites for Optical Imaging and Photothermal Therapy

Xinyi Peng,[⊥,†] Rui Wang,[⊥,‡] Tingjian Wang,[§] Wanning Yang,[†] Hao Wang,[†] Wei Gu,*[,‡] and Ling Ye*[,‡]

[‡]School of Pharmaceutical Sciences, Capital Medical University, Beijing 100069, P. R. China

[†]School of Basic Medical Sciences, Capital Medical University, Beijing 100069, P. R. China

[§]Department of Neurosurgery, Beijing Sanbo Brain Hospital, Capital Medical University, Beijing 100093, P. R. China

Supporting Information

ABSTRACT: Integration of optical imaging modality with photothermal therapy (PTT) for simultaneously providing oncotherapy and bioimaging enables an optimized therapeutic efficacy and higher treatment accuracy and therefore has emerged as a prospective cancer treatment. However, it remains challenging to develop biocompatible PTT nanoagents capable of imaging, monitoring, and diagnosis. Carbon dots (CDs) possess unique photoluminescent (PL) properties and intrinsic biocompatibility; while Prussian blue nanoparticles (PBNPs) are nontoxic with efficient photothermal conversion capacity for PTT. Herein, a simple, cost-effective, and environmentally benign method was developed to strategically fabricate CD-decorated PBNP (CDs/PBNP) nanocomposites with satellite/core structure. The CDs/PBNPs possess distinct green PL emission and near-infrared photoabsorption with high efficiency and photothermal stability. In vitro and in vivo toxicity tests prove the biocompatibility of the CDs/PBNPs. Moreover, the applicability of CDs/PBNPs as nanotheranostic agents was tested, which suggests that CDs/PBNPs possess promising imaging and effective tumor ablation properties.

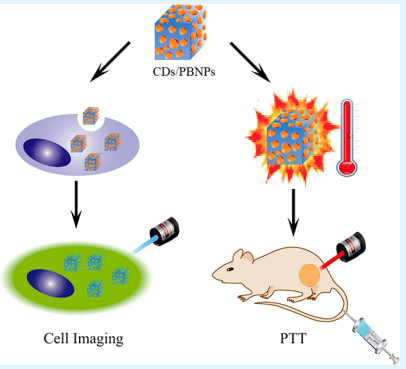

KEYWORDS: *carbon dots/Prussian blue nanoparticles (CDs/PBNPs), photothermal conversion, photoluminescence, optical imaging, photothermal therapy*

1. INTRODUCTION

Despite significant progress in the understanding, diagnosis, treatment, and prevention of cancer, cancer incidence and mortality continues to increase, which demands more efficient and safer therapies in line with surgery, chemotherapy, and radiation therapy for cancer treatments.

During the past few years, photothermal therapy (PTT) has emerged as a prospective adjuvant treatment for cancer.[1] Principally, the implementation of PTT requires a near-infrared (NIR) absorbing agent to induce on-site hyperthermia for irreversible cellular damage or even death of tumor cells. To meet this end, a variety of nanoparticles with photothermal conversion ability have been developed for photothermal ablation of cancer with encouraging outcomes.[2−13] However, the biosafety of the photothermal converting nanoagents remains one major concern for their future clinical use. Recently, Prussian blue nanoparticles (PBNPs) have been employed as a PTT nanoagent due to their excellent NIR absorption properties originating from a metal−metal ion charge transfer from Fe^{2+} to Fe^{3+}.[14−17] More importantly, as a nontoxic and FDA-approved antidote, Prussian blue has been used in clinical settings for scavenging harmful metal ions from the human body.[18,19]

The efficacy of PTT, however, may be limited by ineffective diagnosis and difficulty of overseeing the follow-up therapeutic effect. To overcome this limitation, imaging modality has been integrated into PTT.[20] The added imaging modality enables accurate identification of a tumor's size and location. Meanwhile, it confers a real-time monitor of the therapeutic effect in the region of interest to plan for better intervention, which is essential to improving the therapeutic efficacy. However, it remains challenging to develop biocompatible PTT agents capable of simultaneous imaging and diagnosis in a simple way.

Among various imaging modalities, optical imaging has attracted increasing attention due to its high sensitivity and real-time imaging acquisition. Moreover, optical imaging has been employed for monitoring either the progression of tumors or the response of therapy in a noninvasive fashion. Although organic fluorophors were initially used in optical imaging, the recently developed fluorescent nanoparticles exhibit several advantages over their predecessors,[21] making them excellent alternatives for bioimaging and image-guided therapy. One excellent example of such advancements is carbon dots (CDs), which are luminescent nanomaterials with advantages that include unique photoluminescence (PL)

Received: October 2, 2017
Accepted: December 18, 2017
Published: December 18, 2017

DOI: 10.1021/acsami.7b14972
ACS Appl. Mater. Interfaces 2018, 10, 1084−1092

properties, excellent solubility, chemical inertness, and easy surface manipulation.[22−29] Another extraordinary aspect of fluorescent CDs is the cost-effective and environmentally friendly preparation and intrinsic biocompatibility,[30] which can hardly be realized with conventional semiconducting quantum dots. These distinct features make CDs excellent fluorescent imaging agents for image-guided therapy with enhanced therapeutic efficiency.[31−33]

Herein, we report a simple, cost-effective, and environmentally benign method for fabricating CD/PBNP satellite/core nanocomposites that integrate the distinct PL properties of CDs and high photothermal conversion ability of PBNPs in one single platform. As illustrated in Scheme 1, the CDs were

Scheme 1. Schematic Illustration of Synthesis of CD/PBNP Satellite/Core Nanocomposites for Optical Imaging and PTT

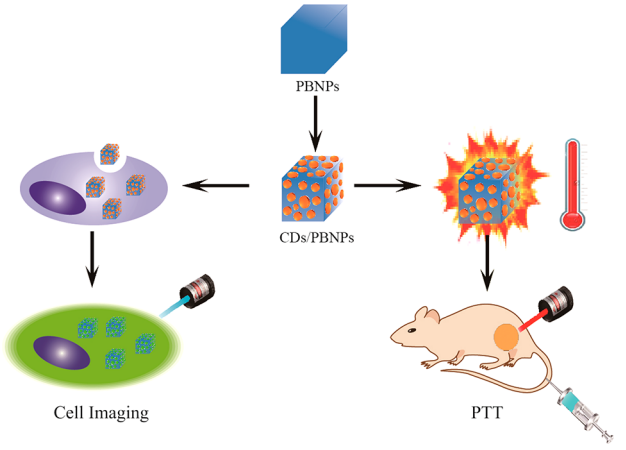

in situ formed on the PBNPs by microwave-assisted carbonation of citric acid, which was used as a capping agent to stabilize the PBNPs. Moreover, urea was introduced as the nitrogen dopant to render the CDs with green PL. The PL properties, photothermal conversion performance, and biocompatibility of CDs/PBNPs were examined. Moreover, the applicability of the CDs/PBNPs as optical nanoprobes for cancer cell imaging and as photothermal conversion nanoagents for PTT of tumors was shown.

2. EXPERIMENTAL SECTION

2.1. Preparation of CDs/PBNPs. The PBNPs were first prepared according to the reported protocol.[34] Then, a one-step microwave-assisted carbonation method[35] was adopted to deposit CDs on PBNPs. Typically, 90 mg of CA, 270 mg of urea, and 10 mg of as-prepared PBNPs were added to 10 mL of DI water in a 50 mL beaker, followed by heating in a 750 W domestic microwave oven (Galanz, China) for 4.5 min. After cooling to room temperature, the yielded solid was suspended in 10 mL of DI water. Then, the suspension was centrifuged (12 000 r/min, 15 min) to obtain the CDs/PBNPs by disposing of the free CDs remaining in the supernatant.

2.2. Cytotoxicity Assay. The cytotoxicity of CDs/PBNPs toward glioma C6 cells was tested according to a standard MTT assay. Three independent experiments were performed to obtain the cell viability, which was expressed as mean ± standard deviation.

2.3. In Vivo Biosafety Analysis. All animal experiments were performed following the protocols evaluated and approved by the ethical committee of Capital Medical University. Healthy ICR mice (n = 3) were injected with 200 μL of CDs/PBNPs at a dosage of 20 mg kg^{-1}. At 15 days postinjection, the mice were anaesthetized, and the eyeballs were removed, followed by collection of blood samples for blood chemistry and routine blood tests. Subsequently, the brain, heart, liver, spleen, lungs, and kidneys of the mice were harvested and fixed with 4% paraformaldehyde. The tissue samples were then embedded, sliced, stained with hematoxylin and eosin (H&E), and examined under a microscope (Leica DM6000B) at 10× magnification. The mice injected with PBS were treated as the control.

2.4. Cell Imaging. The glioma C6 cells on the coverslip were incubated with FBS-free DMEM containing CDs/PBNPs (0.5 mg mL^{-1}) for 12 h. Then, the cells were imaged on a SP5 confocal laser scanning microscope (CLSM, Leica) upon excitation at 405 nm.

2.5. Ex Vivo Fluorescence Imaging. Two hours after injection of CDs/PBNPs (20 mg per kg body weight), the mice were sacrificed, and the major organs (heart, liver, spleen, lungs, kidneys, and brain) were immediately excised and imaged on the Kodak in vivo FX Pro fluorescence imaging system (Kodak, United States).

2.6. Measurement of Photothermal Effect. An 808 nm NIR laser (Beijing Viasho Technology Co., China) was used for the photothermal effect measurements. An aqueous suspension of CDs/PBNPs (1 mL) was placed in a vial at a series of concentrations (0, 0.05, 0.1, 0.2, 0.4, and 0.5 mg mL^{-1}) and was exposed to the NIR laser (808 nm, 0.8 W cm^{-2}) for 10 min. During the irradiation, the temperature of the CDs/PBNPs dispersion was measured by an infrared thermal camera (Fotric 225). The photothermal conversion efficiency (η) was calculated according to the method reported in the literature.[36]

To evaluate the photothermal stability, an aqueous dispersion of CDs/PBNPs (0.4 mg mL^{-1}) was irradiated by an 808 nm laser (0.8 W cm^{-2}) for 5 consecutive laser-on/off cycles. In addition, the UV−vis absorbance and PL emission spectra of CDs/PBNPs before and after five laser-on/laser-off cycles were recorded.

2.7. In Vitro Photothermal Toxicity. To evaluate the photothermal toxicity at the cellular level, C6 cells were incubated with media containing PBS (control) and CDs/PBNPs (0.5 mg mL^{-1}) for 2 h. After an 808 nm NIR irradiation (0.8 W cm^{-2}) for 10 min, the cells were rinsed with PBS, and the live/dead status of cells was examined under an optical microscope.

2.8. In Vivo Photothermal Treatment. C6 cells (2×10^6 cells mL^{-1} in PBS) were subcutaneously injected to the right flanks of nude mice to establish the tumors. Seven days after tumor inoculation, mice were administered intravenously with CDs/PBNPs (200 μL, 2 mg mL^{-1} per mouse per injection). At 12 h postinjection, tumors were irradiated with NIR (808 nm, 0.8 W cm^{-2}) for 10 min. Mice treated with saline with/without laser exposure or injected with CDs/PBNPs without laser exposure were applied as the control groups. To monitor the change of the tumor, the tumor size was measured at predetermined times. The relative tumor volume was then calculated following the method reported elsewhere.[37]

3. RESULTS AND DISCUSSION

3.1. Characterization. The direct microwave-assistant carbonization of the capped citric acid on PBNPs provides a simple, cost-effective, and environmentally benign approach to fabricate CD/PBNP nanocomposites with satellite/core structure. The morphology and size of the PBNPs and CDs/PBNPs were observed from transmission electron microscopy (TEM) images. According to TEM images, the PBNPs have a cubic shape with a size of 50 nm (Figures 1A and B). An increase in size was observed for CDs/PBNPs (Figure 1C), which is further supported by the corresponding size distribution histogram (Figure 1D). Moreover, the edge of CDs/PBNPs became fuzzy. The changes in the morphology and size thus suggest the successful fabrication of the CD/PBNP satellite/core nanocomposites. The presence of Fe and C in the satellite/core CDs/PBNPs was supported by the high-angle annular dark-field scanning transmission electron microscopy (HAADF-STEM) image (Figure S1).

DOI: 10.1021/acsami.7b14972
ACS Appl. Mater. Interfaces 2018, 10, 1084−1092

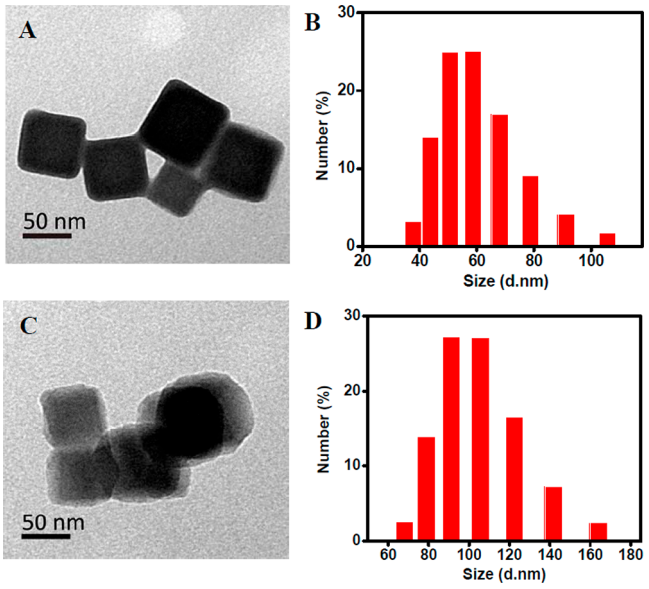

Figure 1. TEM images and size distribution of PBNPs (A and B) and CDs/PBNPs (C and D).

The formed CDs/PBNPs were further characterized by the X-ray diffraction (XRD), Fourier transform infrared (FTIR) spectroscopy, and UV−vis spectroscopy. The powder XRD pattern of CDs/PBNPs (Figure 2A) exhibits characteristic PBNP diffraction peaks at 17.4, 24.5, 35.2, and 39.5°, corresponding to the 200, 220, 400, and 420 planes indexed to cubic face-centered Prussian blue lattices (JCPDS card no. 52-1907) using the space group $Fm\bar{3}m$. Meanwhile, the bump of the baseline together with a peak at 2θ of 26.3° due to the intrinsic graphitic structure indicates the simultaneous presence of CDs, which possess crystalline carbon core and amorphous carbonaceous surface.

The FTIR spectrum of CDs/PBNPs (Figure 2B) shows an intensive band at 2070 cm^{-1} due to the stretching of Fe^{2+}−CN−Fe^{3+} in PBNPs and couples of bands originating from various surface functional groups of CDs such as the broad band at 3300 cm^{-1} due to stretching of −OH and the bands at 1712 and 1364 cm^{-1} assigned to the asymmetric and symmetric stretching of C═O, respectively.

The UV−vis spectrum of CDs/PBNPs presents the broad near-infrared absorption (750−950 nm) due to the charge carrier hopping of Fe^{2+} and Fe^{3+} in the PBNPs (Figure 2C). Note that the NIR absorption of CDs/PBNPs experiences a slight red-shift compared to that of pristine PBNPs. In addition, an absorption around 420 nm originating from the $n-\pi^*$ transition of C═O groups was evidenced. Moreover, the absorbance of these peaks increases with the increasing of CDs/PBNPs concentration (Figure 2D). Overall, the TEM, XRD, FTIR, and UV−vis characterization confirms the successful preparation of CD/PBNP nanocomposites.

3.2. PL Properties. The synthesized CDs/PBNPs could be readily dispersed in water and appeared with the characteristic blue color of PBNPs (inset, Figure 3A). Nevertheless, the incorporated CDs render the nanocomposites with PL properties. Upon excitation at 400 nm, the aqueous dispersion of the CDs/PBNPs emitted strong visible green PL (inset, Figure 3A). Accordingly, the PL emission spectrum of the CDs/PBNPs shows the maximum emission wavelength around 540 nm (Figure 3A). Moreover, the corresponding PL excitation spectrum presents one peak with a position close to that of the absorption band.

Additionally, the PL emission spectra of CDs/PBNPs under excitations from 340 to 460 nm in 20 nm increments were acquired and are illustrated in Figure 3B. Note that the CDs/

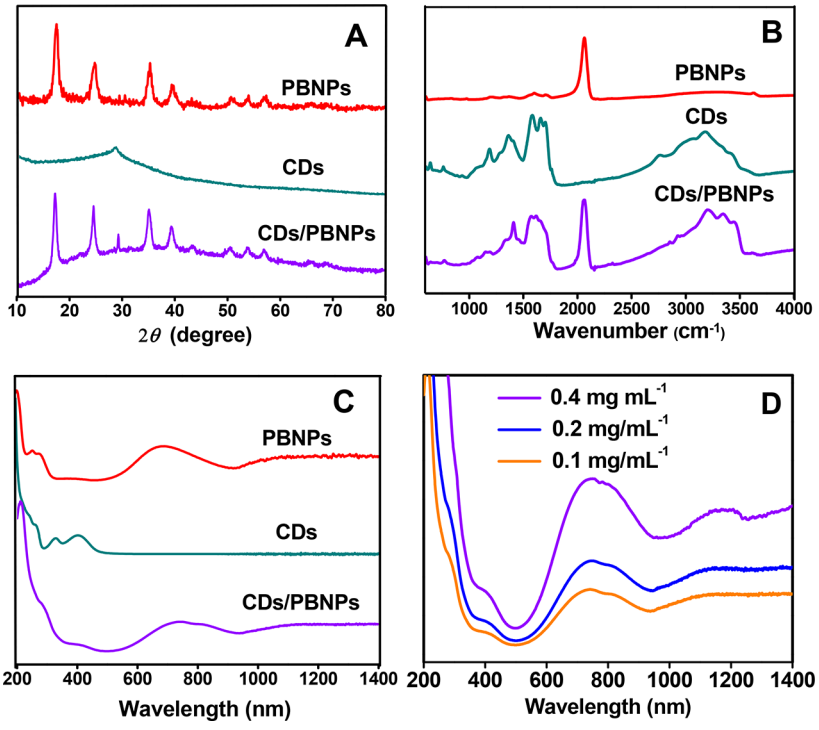

Figure 2. (A) XRD patterns; (B) FTIR spectra; (C) UV−vis spectra of PBNPs, CDs, and CDs/PBNPs; and (D) UV−vis spectra of CDs/PBNPs at different concentrations.

DOI: 10.1021/acsami.7b14972
ACS Appl. Mater. Interfaces 2018, 10, 1084−1092

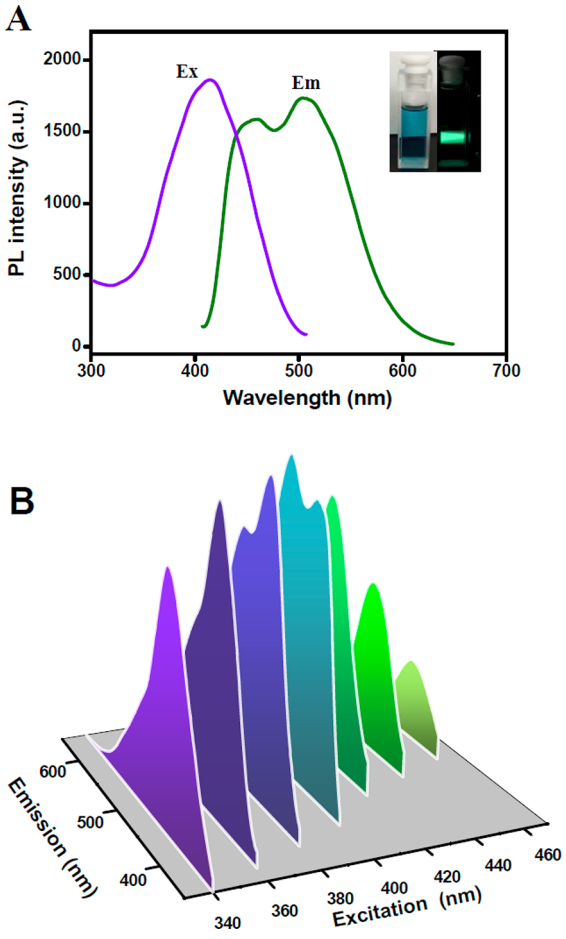

Figure 3. (A) PL emission and excitation spectra of CDs/PBNPs and (B) PL emission spectra of CDs/PBNPs under excitations from 340 to 460 nm in 20 nm increments.

PBNPs exhibit an excitation wavelength-dependent PL emission from blue to green, indicating a variety of PL centers. Moreover, it is found that the PL intensity of CDs/PBNPs increases with increasing of excitation wavelength and then decreases. Consequently, the maximum intensity of green PL emission is achieved upon excitation at 400 nm. The quantum yield (QY) of the CDs/PBNPs under excitation of 400 nm was measured to be about 6.5% using an integrating sphere.

3.3. In Vitro and In Vivo Toxicity. The cytotoxicity of the CDs/PBNPs was tested using the MTT assay. Upon incubation with CDs/PBNPs for 24 h, the viability of C6 cells was determined, and the results are plotted in Figure 4. It was revealed that over 80% of C6 cells survived at all testing concentrations, implying the low cytotoxicity of CDs/PBNPs.

Furthermore, toxicology analysis of CDs/PBNPs was investigated via in vivo blood biochemistry test, blood routine analysis, and H&E staining examination. In the blood biochemistry test, three important hepatic and kidney function indicators, including aminotransferase (AST), aminotransferase (ALT), and creatinine (CRE), were examined. As displayed in Figure 5A, the levels of these markers for the treatment group are almost the same as those of the control groups, verifying the good hepatic and kidney safety profile of CDs/PBNPs. Moreover, standard blood parameters, including red blood cells (RBCs), white blood cells (WBCs), hemoglobin (HGB), platelets (PLT), mean corpuscular volume (MCV), mean corpuscular hemoglobin (MCH),

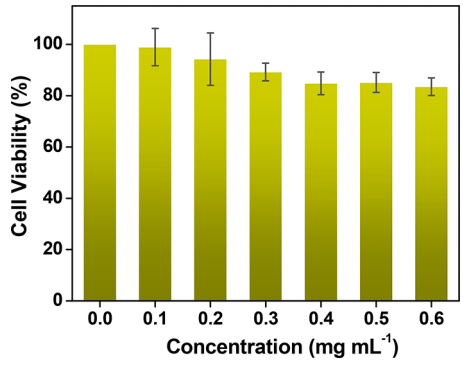

Figure 4. Viability of C6 cells upon incubation with the CDs/PBNPs at varying concentrations for 24 h.

mean platelet volume (MPV), red blood cell distribution width (RDW), lymphocyte count (LYMPH#), lymphocyte percentage (LYMPH%), monocyte percentage (MONO%), and neutrophile percentage (NEUT%) were measured. As expected, all of these parameters are in the normal range, and there is no significant difference from those mice in the control group (Figure 5B), suggesting good hemocompatibility of CDs/PBNPs.

Furthermore, in vivo toxicity of CDs/PBNPs was examined using the H&E staining test. The major organs (brain, heart, liver, spleen, lungs, and kidneys) of ICR mice 7 days after injection of CDs/PBNPs (20 mg kg^{-1}) were harvested and stained with H&E. As presented in Figure 5C, no notable toxicity was observed in the tissues from the animals receiving CDs/PBNPs in comparison with the control group. The histological assessment thus validates that CDs/PBNPs are biocompatible in living mice, which is crucial for in vivo biomedical applications.

3.4. Optical Imaging. Inspired by the unique PL properties and biocompatibility, the feasibility of CDs/PBNPs as optical nanoprobes for bioimaging at the cellular level was first examined. The CLSM images of C6 cells upon incubation of the CDs/PBNPs are shown in Figure 6. As can be seen, under a 405 nm laser excitation, the C6 cells treated with CDs/PBNPs emit green fluorescence primarily from the cytoplasm, suggesting that CDs/PBNPs could be efficiently uptaken by the C6 cells and thereby possess great promise in serving as effective optical nanoprobes for bioimaging purposes.

Next, ex vivo optical imaging was performed to further testify the applicabilities of CDs/PBNPs as optical nanoprobes for bioimaging. Two hours after injection of the CDs/PBNPs, major organs were harvested for fluorescence imaging. As shown in Figure 7, relatively high fluorescence signals are found in the liver, kidneys, and lungs, whereas the spleen and heart show minimum fluorescence signals, which could be attributed to the first pass effect.[38] The accumulation of CDs/PBNPs in kidneys suggests that CDs/PBNPs could be excreted by urine. Interestingly, a considerable amount of the CDs/PBNPs is retained in the brain, implying that the CDs/PBNPs could pass through the blood-brain barrier and therefore have potential in the detection and PTT of brain tumors.

3.5. Photothermal Conversion Performances. In addition to the PL properties, the photothermal conversion performances of the CDs/PBNPs were investigated. Upon an 808 nm NIR laser radiation (0.8 W cm^{-2}, 10 min), an obvious temperature elevation was recorded (Figures 8A and B). In

DOI: 10.1021/acsami.7b14972
ACS Appl. Mater. Interfaces 2018, 10, 1084−1092

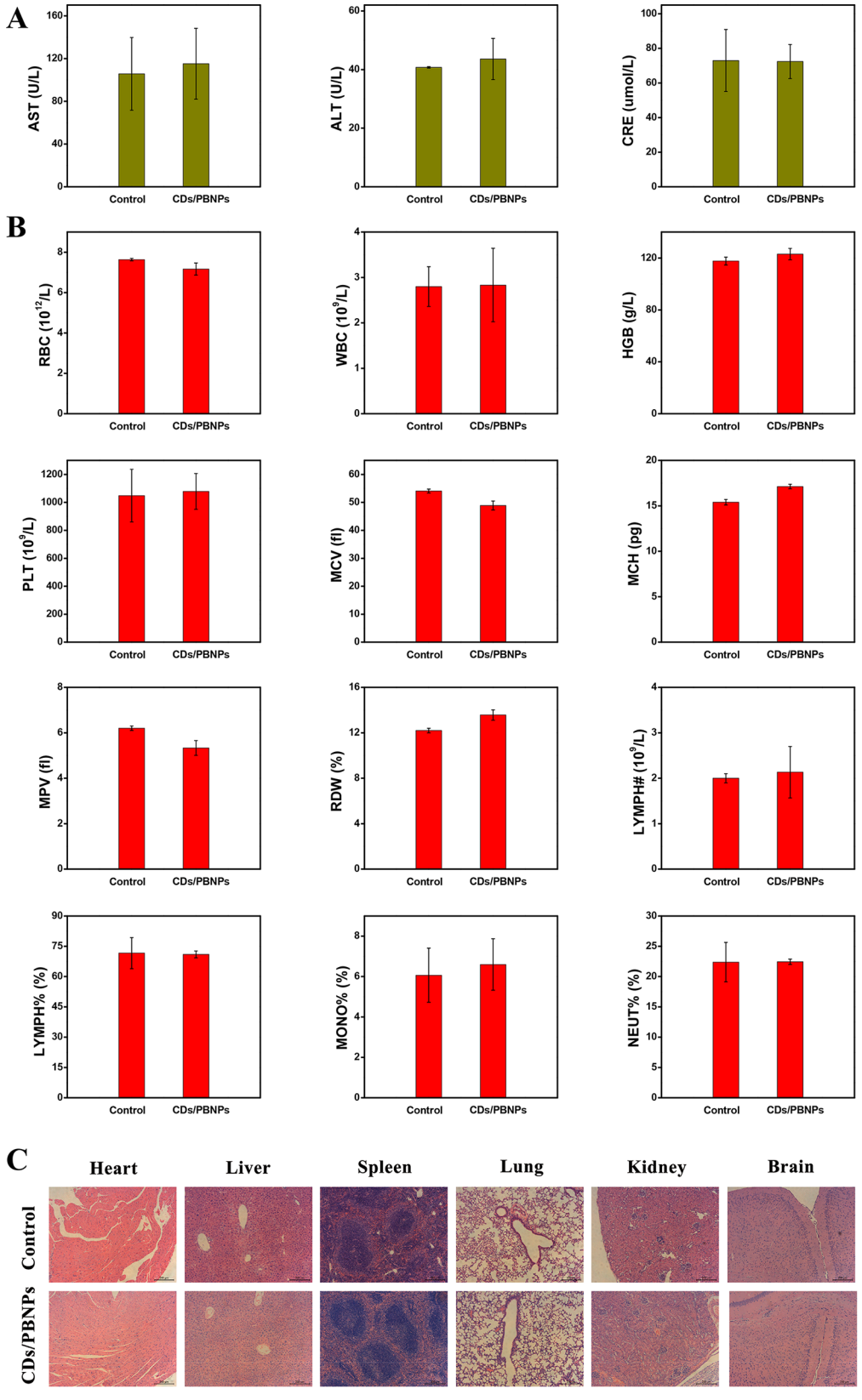

Figure 5. In vivo toxicology assessment of CDs/PBNPs. (A) Blood biochemistry test, (B) routine blood analysis, and (C) H&E-stained tissues (heart, liver, spleen, lungs, kidneys, and brain) from mice treated with saline (control) and CDs/PBNPs, respectively. Scale bars: 200 μm.

contrast, the increase in the temperature of pure water was negligible (about 1.9 °C). This thus verifies the efficient thermal conversion ability of CDs/PBNPs. Moreover, it is noted that the photothermal conversion ability of CDs/PBNPs depends on their concentration as well as the duration of the irradiation. Nevertheless, the temperature of the CDs/PBNPs after 10 min of NIR irradiation is higher than the critical temperature (42 °C) required to kill cancer cells through

DOI: 10.1021/acsami.7b14972
ACS Appl. Mater. Interfaces 2018, 10, 1084−1092

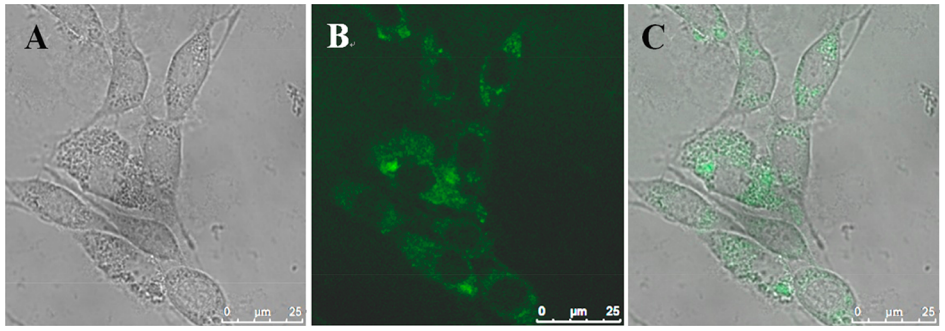

Figure 6. CLSM images of C6 cells incubation with CDs/PBNPs (A) under bright field and (B) under a 405 nm laser excitation. (C) Overlay of A and B. Scale bars: 25 μm.

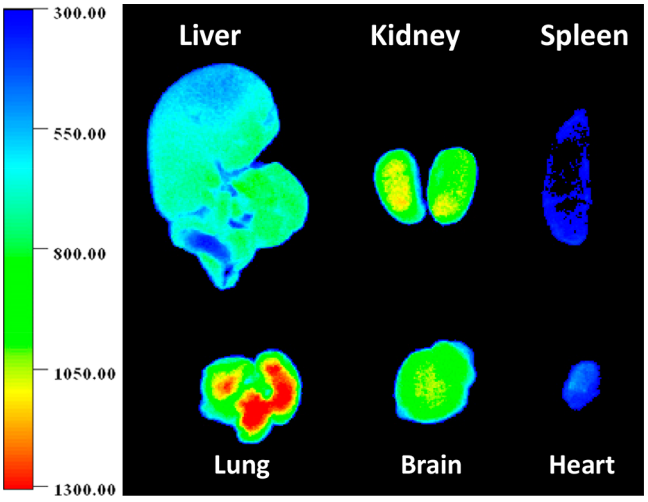

Figure 7. Representative intensity scaled fluorescence images of major organs from mouse injected with the CDs/PBNPs.

photothermal conversion, even at 0.05 mg mL^{-1}, implying a high photothermal conversion efficiency of CDs/PBNPs. Accordingly, the photothermal conversion efficiency of CDs/PBNPs was calculated to be about 30%. Note that this value is comparable to that of native PBNPs reported in literature,[15] suggesting that the CDs have minor effect on the photothermal conversion of PBNPs.

Besides, photothermal stability is another key consideration for a photothermal conversion agent. To probe the photothermal stability of the CDs/PBNPs, cyclic photothermal conversion was conducted. As shown in Figure 8C, over 5 consecutive laser-on/laser-off cycles, the photothermal conversion performance of the CDs/PBNPs (0.4 mg mL^{-1}) remained consistently robust, clearly validating the photothermal stability of the CDs/PBNPs. Moreover, no significant change in the UV−vis absorption and PL emission spectra of CDs/PBNPs was observed after irradiation after five laser-on/laser-off cycles (Figure S2). Overall, the high photothermal conversion efficiency and the outstanding photothermal

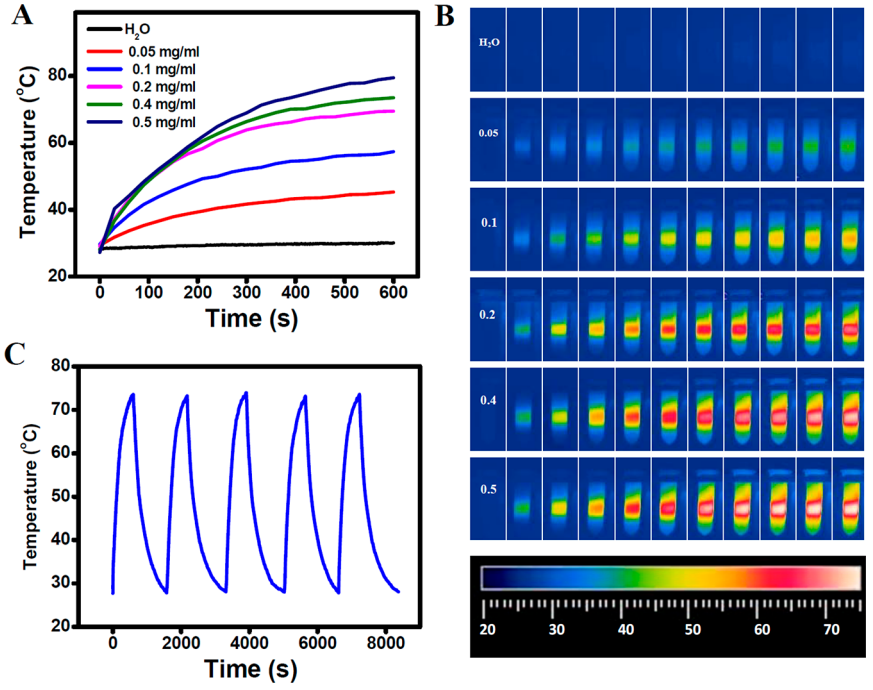

Figure 8. (A) Photothermal conversion of CDs/PBNPs at different concentration. (B) corresponding IR thermographic images acquired at 0, 1, 2, 3, 4, 5, 6, 7, 8, 9, and 10 min (from left to right). (C) photothermal stability of CDs/PBNPs for five consecutive cycles.

DOI: 10.1021/acsami.7b14972
ACS Appl. Mater. Interfaces 2018, 10, 1084−1092

stability thereby confirm the effectiveness of CDs/PBNPs as photothermal conversion agents.

3.6. In Vitro Photothermal Toxicity toward Tumor Cells. Next, the feasibility of the CDs/PBNPs for photothermal killing of tumor cells was first explored. The brain glioma C6 cells were employed in this study as a model to evaluate the in vitro photothermal toxicity of the CDs/PBNPs. As shown in Figure 9, an NIR laser exposure (808 nm, 0.8 W cm^{-2}, 10 min) exerted only negligible photothermal damage to the control C6 cells (Figures 9A and B). In contrast, NIR irradiation of C6 cell incubation with the CDs/PBNPs led to notable photothermal ablation of C6 cells (Figures 9C and D) due to the high photothermal conversion capacity of the CDs/PBNPs, which produces enough heat to cause the irreversible damage of tumor cells, either through loosening the cell membranes or denaturing the proteins.[39]

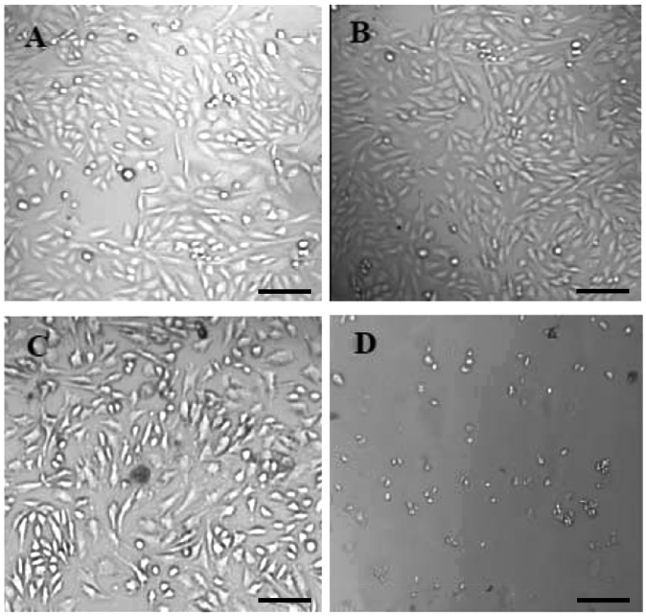

Figure 9. Photothermal toxicity of CDs/PBNPs toward (A) C6 cells, (B) C6 cells after laser radiation, (C) C6 cells with CDs/PBNPs, and (D) C6 cells with CDs/PBNPs after laser radiation. Scale bars: 50 μm.

3.7. In Vivo Tumor Photothermal Treatment. Furthermore, the PTT efficacy of CDs/PBNPs was examined on tumor-bearing mice. Figure 10A provides the real-time IR thermal photos of saline and CDs/PBNPs (20 mg kg^{-1}) treated tumor-bearing mice exposed to 808 nm laser (0.8 W cm^{-2}) for 10 min. Due to strong absorption at 808 nm and efficient photothermal conversion ability, the tumor temperature of mice injected with the CDs/PBNPs rapidly elevated to around 55 °C under laser irradiation, which was high enough to effectively ablate tumors. Consequently, 2 days after laser irradiation, a remarkable regression of the tumor was observed (Figure 10A). In contrast, no notable therapeutic effect was observed in the control groups (Figure 10B). The therapeutic efficacy was further supported the tumor growth measured every 2 days after treatment (Figure S3). The tumor growth on CDs/PBNPs + NIR mice were efficiently suppressed, whereas, neither NIR irradiation nor CDs/PBNPs alone would affect the tumor growth. Nevertheless, the body weight of the mice treated with CDs/PBNPs and laser exposure remained stable, suggesting no systemic side effects during PTT. Taken together, it can be concluded that the CDs/PBNPs could act as powerful and efficient photothermal conversion nanoagents for tumor PTT.

4. CONCLUSION

In summary, the CD/PBNP satellite/core nanocomposites combining unique PL properties of CDs and photothermal conversion ability of PBNPs were successful prepared by in situ growth of CDs on PBNPs through a simple microwave-assisted synthesis method. The CDs/PBNPs emit excitation wavelength-dependent PL and could efficiently illuminate C6 tumor cells. Meanwhile, the CDs/PBNPs possess high photothermal conversion efficiency (~30%) and are extremely photothermal stable. In addition, the CDs/PBNPs exhibit effective photothermal cytotoxicity toward C6 cells and photothermal therapeutic effect for tumor-bearing mice. Therefore, the CDs/PBNPs combining the optical imaging modality and the PTT capacity hold great potential in imaging guidance and PTT treatment of tumor with improved efficacy.

■ ASSOCIATED CONTENT

Supporting Information

The Supporting Information is available free of charge on the ACS Publications website at DOI: 10.1021/acsami.7b14972.

Experimental details, HAADF-STEM image, EDX spectrum, UV−vis and PL emission spectra, and tumor growth curves (PDF)

■ AUTHOR INFORMATION

Corresponding Authors

*E-mail: lingye@ccmu.edu.cn.
*E-mail: weigu@ccmu.edu.cn.

ORCID

Wei Gu: 0000-0001-5908-1616

Author Contributions

⊥X.P. and R.W. contributed equally to this work.

Notes

The authors declare no competing financial interest.

■ ACKNOWLEDGMENTS

The authors gratefully acknowledge financial support from the Key Project from Beijing Commission of Education (Grant KZ201610025022), National Natural Science Foundation of China (Grant 81271639), and the Beijing Natural Science Foundation (Grant 7162023). The authors also acknowledge technical support from the Core Facility Center (CFC) at Capital Medical University.

■ REFERENCES

(1) Zou, L.; Wang, H.; He, B.; Zeng, L.; Tan, T.; Cao, H.; He, X.; Zhang, Z.; Guo, S.; Li, Y. Current approaches of photothermal therapy in treating cancer metastasis with nanotherapeutics. *Theranostics* **2016**, *6*, 762−772.

(2) de Melo-Diogo, D.; Pais-Silva, C.; Dias, D. R.; Moreira, A. F.; Correia, I. J. Strategies to improve cancer photothermal therapy mediated by nanomaterials. *Adv. Healthcare Mater.* **2017**, *6*, 1700073.

(3) Cano-Mejia, J.; Burga, R. A.; Sweeney, E. E.; Fisher, J. P.; Bollard, C. M.; Sandler, A. D.; Cruz, C. R. Y.; Fernandes, R. Prussian blue nanoparticle-based photothermal therapy combined with checkpoint inhibition for photothermal immunotherapy of neuroblastoma. *Nanomedicine* **2017**, *13*, 771−781.

DOI: 10.1021/acsami.7b14972
ACS Appl. Mater. Interfaces 2018, 10, 1084−1092

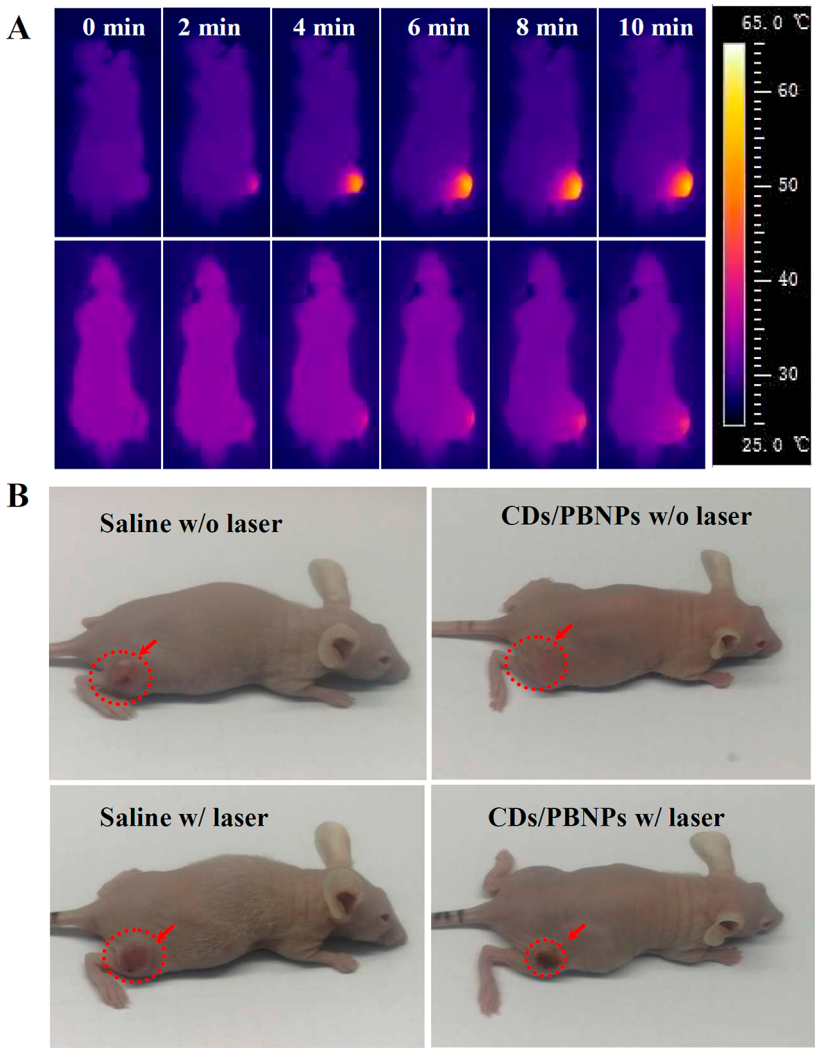

Figure 10. (A) IR thermal images of tumor-bearing mice treated with CDs/PBNPs and saline under an 808 nm laser (0.8 W cm^{-2}) irradiation. (B) Photos of tumor-bearing mice two days after saline injection without laser exposure, CDs/PBNPs injection without laser exposure, saline injection with laser exposure, and CDs/PBNPs injection with laser exposure.

(4) Jaque, D.; Maestro, L. M.; Del Rosal, B.; Haro-Gonzalez, P.; Benayas, A.; Plaza, J.; Rodriguez, E. M.; Sole, J. G. Nanoparticles for photothermal therapies. *Nanoscale* **2014**, *6*, 9494−9530.
(5) Abbas, M.; Zou, Q.; Li, S.; Yan, X. Self-assembled peptide-and protein-based nanomaterials for antitumor photodynamic and photothermal therapy. *Adv. Mater.* **2017**, *29*, 1605021.
(6) Shi, Y.; Liu, M.; Deng, F.; Zeng, G.; Wan, Q.; Zhang, X.; Wei, Y. Recent progress and development on polymeric nanomaterials for photothermal therapy: a brief overview. *J. Mater. Chem. B* **2017**, *5*, 194−206.
(7) Chen, Y.; Wang, L.; Shi, J. Two-dimensional non-carbonaceous materials-enabled efficient photothermal cancer therapy. *Nano Today* **2016**, *11*, 292−308.
(8) Chen, Y.-W.; Su, Y.-L.; Hu, S.-H.; Chen, S.-Y. Functionalized graphene nanocomposites for enhancing photothermal therapy in tumor treatment. *Adv. Drug Delivery Rev.* **2016**, *105*, 190−204.
(9) Zou, Q.; Abbas, M.; Zhao, L.; Li, S.; Shen, G.; Yan, X. Biological photothermal nanodots based on self-assembly of peptide porphyrin conjugates for antitumor therapy. *J. Am. Chem. Soc.* **2017**, *139*, 1921−1927.
(10) Jia, Q.; Ge, J.; Liu, W.; Zheng, X.; Wang, M.; Zhang, H.; Wang, P. Biocompatible iron phthalocyanine-albumin assemblies as photoacoustic and thermal theranostics in living mice. *ACS Appl. Mater. Interfaces* **2017**, *9*, 21124−21132.
(11) Zhu, H.; Lai, Z.; Fang, Y.; Zhen, X.; Tan, C.; Qi, X.; Ding, D.; Chen, P.; Zhang, H.; Pu, K. Ternary chalcogenide nanosheets with ultrahigh photothermal conversion efficiency for photoacoustic theranostics. *Small* **2017**, *13*, 1604139.
(12) Zhu, H.; Fang, Y.; Miao, Q.; Qi, X.; Ding, D.; Chen, P.; Pu, K. Regulating Near-Infrared Photodynamic Properties of semiconducting polymer nanotheranostics for optimized cancer therapy. *ACS Nano* **2017**, *11*, 8998−9009.
(13) Lyu, Y.; Fang, Y.; Miao, Q.; Zhen, X.; Ding, D.; Pu, K. Intraparticle Molecular orbital engineering of semiconducting polymer nanoparticles as amplified theranostics for in vivo photoacoustic imaging and photothermal therapy. *ACS Nano* **2016**, *10*, 4472−4481.
(14) Fu, G.; Liu, W.; Feng, S.; Yue, X. Prussian blue nanoparticles operate as a new generation of photothermal ablation agents for cancer therapy. *Chem. Commun.* **2012**, *48*, 11567−11569.
(15) Hoffman, H. A.; Chakrabarti, L.; Dumont, M. F.; Sandler, A. D.; Fernandes, R. Prussian blue nanoparticles for laser-induced photothermal therapy of tumors. *RSC Adv.* **2014**, *4*, 29729−29734.
(16) Fu, G.; Liu, W.; Li, Y.; Jin, Y.; Jiang, L.; Liang, X.; Feng, S.; Dai, Z. Magnetic Prussian blue nanoparticles for targeted photothermal therapy under magnetic resonance imaging guidance. *Bioconjugate Chem.* **2014**, *25*, 1655−1663.

DOI: 10.1021/acsami.7b14972
ACS Appl. Mater. Interfaces 2018, 10, 1084−1092

(17) Yang, Y.; Jing, L.; Li, X.; Lin, L.; Yue, X.; Dai, Z. Hyaluronic acid conjugated magnetic Prussian blue@quantum dot nanoparticles for cancer theranostics. *Theranostics* **2017**, *7*, 466−481.
(18) Shokouhimehr, M.; Soehnlen, E. S.; Hao, J.; Griswold, M.; Flask, C.; Fan, X.; Basilion, J. P.; Basu, S.; Huang, S. D. Dual purpose Prussian blue nanoparticles for cellular imaging and drug delivery: a new generation of T_1-weighted MRI contrast and small molecule delivery agents. *J. Mater. Chem.* **2010**, *20*, 5251−5259.
(19) Yang, H.; Sun, L.; Zhai, J.; Li, H.; Zhao, Y.; Yu, H. In situ controllable synthesis of magnetic Prussian blue/graphene oxide nanocomposites for removal of radioactive cesium in water. *J. Mater. Chem. A* **2014**, *2*, 326−332.
(20) Chen, Q.; Wen, J.; Li, H.; Xu, Y.; Liu, F.; Sun, S. Recent advances in different modal imaging-guided photothermal therapy. *Biomaterials* **2016**, *106*, 144−166.
(21) Palner, M.; Pu, K.; Shao, S.; Rao, J. Semiconducting polymer nanoparticles with persistent near-infrared luminescence for in vivo optical imaging. *Angew. Chem., Int. Ed.* **2015**, *54*, 11477−11480.
(22) Teradal, N. L.; Jelinek, R. Carbon nanomaterials in biological studies and biomedicine. *Adv. Healthcare Mater.* **2017**, *6*, 1700574.
(23) Shah, S. N. A.; Lin, J.-M. Recent advances in chemiluminescence based on carbonaceous dots. *Adv. Colloid Interface Sci.* **2017**, *241*, 24−36.
(24) Shen, L.-M.; Liu, J. New development in carbon quantum dots technical applications. *Talanta* **2016**, *156*, 245−256.
(25) Sun, Y.-P.; Zhou, B.; Lin, Y.; Wang, W.; Fernando, K. S.; Pathak, P.; Meziani, M. J.; Harruff, B. A.; Wang, X.; Wang, H. Quantum-sized carbon dots for bright and colorful photoluminescence. *J. Am. Chem. Soc.* **2006**, *128*, 7756−7757.
(26) Yang, S.-T.; Cao, L.; Luo, P. G.; Lu, F.; Wang, X.; Wang, H.; Meziani, M. J.; Liu, Y.; Qi, G.; Sun, Y.-P. Carbon dots for optical imaging in vivo. *J. Am. Chem. Soc.* **2009**, *131*, 11308−11309.
(27) Cao, L.; Wang, X.; Meziani, M. J.; Lu, F.; Wang, H.; Luo, P. G.; Lin, Y.; Harruff, B. A.; Veca, L. M.; Murray, D. Carbon dots for multiphoton bioimaging. *J. Am. Chem. Soc.* **2007**, *129*, 11318−11319.
(28) Baker, S. N.; Baker, G. A. Luminescent carbon nanodots: emergent nanolights. *Angew. Chem., Int. Ed.* **2010**, *49*, 6726−6744.
(29) Ostadhossein, F.; Pan, D. Functional carbon nanodots for multiscale imaging and therapy. *Wiley Interdiscip. Rev.: Nanomed. Nanobiotechnol.* **2017**, *9*, e1436.
(30) Liu, J.-H.; Yang, S.-T.; Chen, X.-X.; Wang, H. Fluorescent carbon dots and nanodiamonds for biological imaging: Preparation, application, pharmacokinetics and toxicity. *Curr. Drug Metab.* **2012**, *13*, 1046−1056.
(31) Li, N.; Than, A.; Sun, C.; Tian, J.; Chen, J.; Pu, K.; Dong, X.; Chen, P. Monitoring dynamic cellular redox homeostasis using fluorescence-switchable graphene quantum dots. *ACS Nano* **2016**, *10*, 11475−11482.
(32) Feng, T.; Ai, X.; Ong, H.; Zhao, Y. Dual-responsive carbon dots for tumor extracellular microenvironment triggered targeting and enhanced anticancer drug delivery. *ACS Appl. Mater. Interfaces* **2016**, *8*, 18732−18740.
(33) Feng, T.; Ai, X.; An, G.; Yang, P.; Zhao, Y. Charge-convertible carbon dots for imaging guided drug delivery with enhanced in vivo cancer therapeutic efficiency. *ACS Nano* **2016**, *10*, 4410−4420.
(34) Li, Z.; Hu, Y.; Jiang, T.; Howard, K. A.; Li, Y.; Fan, X.; Sun, Y.; Besenbacher, F.; Yu, M. Human-serum-albumin-coated Prussian blue nanoparticles as pH-/thermotriggered drug-delivery vehicles for cancer thermochemotherapy. *Part Part Syst. Char* **2016**, *33*, 53−62.
(35) Gong, N.; Wang, H.; Li, S.; Deng, Y.; Chen, X. a.; Ye, L.; Gu, W. Microwave-Assisted Polyol Synthesis of Gadolinium-Doped Green Luminescent Carbon Dots as a Bimodal Nanoprobe. *Langmuir* **2014**, *30*, 10933−10939.
(36) Roper, D. K.; Ahn, W.; Hoepfner, M. Microscale heat transfer transduced by surface plasmon resonant gold nanoparticles. *J. Phys. Chem. C* **2007**, *111*, 3636−3641.
(37) Cheng, L.; Gong, H.; Zhu, W.; Liu, J.; Wang, X.; Liu, G.; Liu, Z. PEGylated Prussian blue nanocubes as a theranostic agent for simultaneous cancer imaging and photothermal therapy. *Biomaterials* **2014**, *35*, 9844−9852.
(38) Tansi, F. L.; Rueger, R.; Kollmeier, A. M.; Boehm, C.; Kontermann, R. E.; Teichgraeber, U. K.; Fahr, A.; Hilger, I. A fast and effective determination of the biodistribution and subcellular localization of fluorescent immunoliposomes in freshly excised animal organs. *BMC Biotechnol.* **2017**, *17*, 8.
(39) Markovic, Z. M.; Harhaji-Trajkovic, L. M.; Todorovic-Markovic, B. M.; Kepić, D. P.; Arsikin, K. M.; Jovanović, S. P.; Pantovic, A. C.; Dramićanin, M. D.; Trajkovic, V. S. In vitro comparison of the photothermal anticancer activity of graphene nanoparticles and carbon nanotubes. *Biomaterials* **2011**, *32*, 1121−1129.

DOI: 10.1021/acsami.7b14972
ACS Appl. Mater. Interfaces 2018, 10, 1084−1092